IET Signal Processing

Research Article

IET Journals
The Institution of Engineering and Technology

High-resolution time delay estimation via sparse parameter estimation methods

ISSN 1751-9675
Received on 21st June 2019
Revised 18th November 2019
Accepted on 28th November 2019
E-First on 9th January 2020
doi: 10.1049/iet-spr.2019.0291
www.ietdl.org

Hyung-Rae Park[1] ✉, *Jian Li*[2]

[1]*Department of Electronics and Information Engineering, Korea Aerospace University, 200-1 Hwajeon-dong, Dukyang-gu, Goyang, Republic of Korea*

[2]*Department of Electrical and Computer Engineering, University of Florida, Gainesville, FL 32611, USA*

✉ *E-mail: hrpark@kau.ac.kr*

Abstract: This study addresses the high-resolution time delay estimation (TDE) via sparse parameter estimation methods. Two representative algorithms, Sparse Asymptotic Minimum Variance (SAMV) and SParse Iterative Covariance-based Estimation are devised in both the time and frequency domains for application to the TDE of spread-spectrum signals and their performances are analysed in various multipath environments. The authors also proposes the combined approach of SAMV and weighted RELAX, referred to as SAMV-WRELAX, to reduce the computational load. Numerical examples demonstrate that the frequency-domain approaches with a proper type of snapshots not only outperform the corresponding time-domain approaches but also mitigate the problem of the noise correlation encountered in time-domain processing. They also show that the computational load of SAMV-WRELAX with a grid size of $0.1T_c$ decreases up to a few tenths of that of SAMV with a fine grid, e.g. a size of $0.01T_c$, without any performance degradations.

1 Introduction

Time delay estimation (TDE) plays an important role in many fields including radar, sonar, radio navigation, wireless communication, and geophysical/seismic exploration. Specifically, accurate TDE is crucial to source localising systems such as global navigation satellite systems and real-time locating systems (RTLSs) [1]. Since the accuracy of TDE increases in proportion to the signal bandwidth, the direct-sequence spread spectrum (DS-SS) or ultra-wide bandwidth (UWB) scheme is employed in most source localising systems. A traditional approach to the TDE problem is the correlation method in which the signal received from a single sensor is correlated with the known transmitted signal and the peaks of the correlation outputs are determined as the signal delays. The correlation method can be implemented in a simple way but its resolution capability is limited by the reciprocal of the signal bandwidth.

The problem of TDE can be regarded as a special case of the harmonic retrieval problems that are well studied in the literature. Therefore, the high-resolution algorithms that were originally proposed for spectral estimation or direction-of-arrival (DOA) estimation can be applied to the TDE of closely spaced signals [2–11]. Various algorithms, such as multiple signal classification [2–4], estimation of signal parameters via rotational invariance techniques (ESPRIT) [5, 6], maximum-likelihood (ML) method [7, 8], and minimum entropy [9] were applied to achieve high-resolution TDE. Among them, the ML method provides the best performance but its main drawback is that it is computationally intensive due to the complicated multi-dimensional optimisation of a non-linear least squares (NLSs) criterion. Computationally efficient approaches that decouple the complicated multi-dimensional optimisation problem into a sequence of multiple one-dimensional optimisation problems were proposed in [10, 11]. While most of the high-resolution algorithms stated above perform well in mild situations, they fail to resolve the signals when the signal-to-noise ratio (SNR) is low or the available snapshots are limited. Moreover, they require a prior knowledge for the number of signals, which can be estimated usually by information-theoretic criteria [12]. However, the accuracy of order determination degrades significantly in challenging scenarios.

Sparse parameter estimation methods have attracted much interest in many areas, including statistics [13, 14], radar imaging [15, 16], array processing [17–23] and so on. They are known to have a number of advantages over the aforementioned high-resolution algorithms, such as insensitivity to noise statistics and robustness to signal correlations and limited data. However, many of them require the difficult selection of one or more hyperparameters [13, 14, 17] and special software packages are needed to solve the relevant optimisation problems as well [24], which may limit their use in practical systems. Hyperparameter-free iterative adaptive approach (IAA) based on minimising the weighted least squares cost function was introduced for array processing and spectral analysis [16, 19]. IAA is robust to signal correlations, converges fast in a few iterations, and operates well even with a single snapshot. Another hyperparameter-free algorithm is SParse Iterative Covariance-based Estimation (SPICE), which is based on the minimisation of a sparse covariance fitting criterion [20, 21]. SPICE can provide better performance than previous sparse estimation algorithms including IAA in many challenging scenarios. Also, a series of the hyperparameter-free sparse asymptotic minimum variance (SAMV) approaches based on the minimisation of the asymptotic minimum variance (AMV) criterion were introduced in [23]. It was demonstrated in [23] that AMV is asymptotically equivalent to the ML estimator. The hyperparameter-free sparse estimation algorithms stated above require neither the prior knowledge for the number of signals nor any special software package to solve the relevant optimisation problems [24].

Recently, various sparse estimation algorithms were extended to solve the TDE problem [25–27]. However, they have been devised mostly in the time domain, where the correlation samples are used directly to form snapshots and their performances are sometimes influenced significantly by the noise correlation between adjacent samples. Moreover, some of them suffer from severe performance degradations in coherent signal cases [26]. They require a sufficiently fine grid to obtain the desired performance, which makes them computationally intensive. They also suffer from the plateau effect due to the grid size limitation, which becomes severe when a coarse grid is used simply to reduce the computational load.

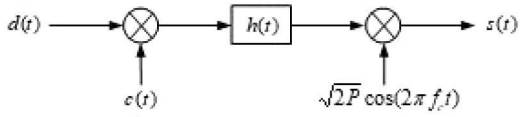

Fig. 1 *BPSK DS-SS transmitter*

In this paper, two representative sparse parameter estimation methods, SAMV and SPICE are devised for high-resolution TDE in both the time and frequency domains, and their performances are analysed with application to the ISO/IEC 24730-2 RTLS (Part 21). Two types of snapshots are considered for frequency-domain processing; one is formed directly with the discrete Fourier transform (DFT) bins obtained from the correlation samples, while the other consists of the DFT bins divided by the known signal spectrum to make the steering matrix a Vandermonde matrix. The former will be more effective for the algorithms which are robust to signal correlations, whereas the latter will be more useful when rank recovery through covariance averaging is necessary. We also propose the SAMV-WRELAX algorithm to reduce the computational load, in which the time delay estimates obtained by SAMV with a coarse grid are used as the initial values for the last step of WRELAX [10, 11].

The remaining part of this paper is organised as follows. Section 2 presents the signal models of spread-spectrum systems in both the time and frequency domains along with a discussion on the correlator output statistics. In Section 3, SAMV and SPICE are introduced for application to the high-resolution TDE and then the computationally efficient SAMV-WRELAX algorithm is proposed. Numerical examples are provided in Section 4 to demonstrate the superiority of the frequency-domain algorithms to the corresponding time-domain algorithms and the computational efficiency of the SAMV-WRELAX algorithm. Finally, Section 5 concludes the paper.

Notation: Vectors and matrices are written in bold italic lower case and upper case characters, respectively. Defined variables are signified by $\triangleq$. $\mathbb{R}$ and $\mathbb{C}$ denote the real and complex planes, respectively. The superscripts T, H, and * stand for transpose, conjugate transpose, and complex conjugate, respectively. $\boldsymbol{R}^{1/2}$ is a matrix square-root of $\boldsymbol{R}$ and $\boldsymbol{R}^{-1/2}$ is its inverse. $\|\cdot\|$ denotes the Euclidian norm for vectors and the Frobenius norm for matrices, and $|\cdot|$ represents the absolute value. $E[\cdot]$ and $\mathrm{tr}[\cdot]$ are the expectation and trace operators, respectively. $\mathrm{vec}(\cdot)$ is the vectorisation operator that stacks all columns on top of one another and $\otimes$ denotes the Kronecker product. $\mathbf{I}_N$ is the $(N \times N)$ identity matrix and $\mathrm{diag}(a_1, \ldots, a_n)$ denotes a diagonal matrix whose diagonal is given by $(a_1, \ldots, a_n)$.

2 Signal models

2.1 Time-domain model

Fig. 1 illustrates the block diagram of a BPSK DS-SS transmitter, where $d(t)$ denotes the data sequence, $c(t)$ the spreading code sequence with a period equivalent to the symbol duration T_s, $h(t)$ the impulse response of a pulse-shaping filter, P the signal power, f_c the carrier frequency. The transmitted signal can be expressed as

$$s(t) = \sqrt{2P} \sum_{\tilde{m}=-\infty}^{\infty} c_{\tilde{m}} d_{\lfloor \tilde{m}/F \rfloor} h(t - \tilde{m}T_c)\cos(2\pi f_c t) \tag{1}$$

where $\lfloor x \rfloor$ represents the integer nearest to x toward $-\infty$, $d_m \in \{1, -1\}$ the mth symbol, $c_{\tilde{m}} \in \{1, -1\}$ the $\tilde{m}$th chip of the code sequence, T_c the chip duration, F the processing gain which is given by T_s/T_c. The baseband signal at the receiver, after I/Q down-conversion, is then represented as

$$r(t) = \sqrt{P} \sum_{l=1}^{L} \alpha_l(t)\, \mathrm{e}^{\mathrm{j}\varphi_l(t)} \sum_{\tilde{m}=-\infty}^{\infty} c_{\tilde{m}} d_{\lfloor \tilde{m}/F \rfloor} h(t - \tilde{m}T_c - \tau_l) + \varepsilon(t) \tag{2}$$

where $\alpha_l(t)$ and $\varphi_l(t)$ are the gain and the phase of the fading channel for the lth signal, respectively, τ_l the propagation delay, and $\varepsilon(t)$ is a zero-mean white Gaussian noise process with double-sided spectral density $N_o/2$. Assuming that the receiver employs a matched filter with impulse response of $h(-t)$, the correlation outputs during the mth symbol period can be expressed as [28]

$$y(t) \simeq F d_m \sqrt{P} \sum_{l=1}^{L} \alpha_l(t)\, \mathrm{e}^{\mathrm{j}\varphi_l(t)} \gamma(t - mT_s - \tau_l) + n(t) \tag{3}$$

where

$$\gamma(t) = \int_{-\infty}^{\infty} \left| H(f) \right|^2 \cos(2\pi f t)\, \mathrm{d}f\,. \tag{4}$$

$H(f)$ is the Fourier transform of $h(t)$ and $n(t)$ involves the background noise, multipath interference, and interchip interference. When the correlator is unsynchronised with all input signals, the variance of $n(t)$ approximates to [28]

$$E[|n(t)|^2] \simeq \frac{F}{T_c}\left\{ N_o \int_{-\infty}^{\infty} \left| H(f) \right|^2 \mathrm{d}f + P \sum_{l=1}^{L} E[\alpha_l^2(t)] \int_{-\infty}^{\infty} \left| H(f) \right|^4 \mathrm{d}f \right\}, \tag{5}$$

where the first part of the right side is due to the background noise and the second part corresponds to the multipath interference. The interchip interference is generally negligible compared with the background noise or multipath interference. Without loss of generality, we assume $\gamma(0) = \int_{-\infty}^{\infty} \left| H(f) \right|^2 \mathrm{d}f = 1$. In order to estimate the delays of the signals with a short duration, a passive correlator should be employed to obtain the correlation samples as fast as possible. Assuming that the tap spacing of the passive correlator is ΔT, $FT_c/\Delta T$ correlation samples are obtained during each symbol period. In order to increase resolution capability, further processing can be applied to the correlation samples. Considering the region of possible delays, we can take N samples around the correlation peaks, which will be used as a snapshot in time-domain processing. Selecting correlation samples not only reduces the region of interest but also filters out all undesired signals outside the region, if any. Assuming that the delays do not change during the measurement, the selected samples during the mth symbol period can be expressed in the following vector form:

$$\boldsymbol{y}(m) = \boldsymbol{A}\boldsymbol{s}(m) + \boldsymbol{n}(m), \quad m = 1, \ldots, M, \in \mathbb{C}^{(N \times 1)}, \tag{6}$$

where $\boldsymbol{A} = [\boldsymbol{a}(\tau_1), \ldots, \boldsymbol{a}(\tau_L)] \in \mathbb{R}^{(N \times L)}$. $\boldsymbol{a}(\tau_l)$ is a known function of τ_l, which is given by

$$\boldsymbol{a}(\tau_l) = [\gamma(t_0 - \tau_l), \gamma(t_1 - \tau_l), \ldots, \gamma(t_{N-1} - \tau_l)]^{\mathrm{T}} \tag{7}$$

with $t_n = n\Delta T, n = 0, 1, \ldots, (N-1)$. The signal vector can be written as

$$\boldsymbol{s}(m) = F d_m \sqrt{P}[\alpha_{1,m}\, \mathrm{e}^{\mathrm{j}\varphi_{1,m}}, \ldots, \alpha_{L,m}\, \mathrm{e}^{\mathrm{j}\varphi_{L,m}}]^{\mathrm{T}}\,. \tag{8}$$

Since $\alpha_{l,m}$ and $\varphi_{l,m}$ depend rarely on the symbol index m in multipath environments, the covariance matrix of $\boldsymbol{s}(m)$ has rank equal to 1. Time-domain approaches make use of the snapshots expressed by (6) and (7) to achieve their high-resolution potential. However, it should be noted that the adjacent elements of $\boldsymbol{n}(m)$ are substantially correlated with a degree depending on ΔT. In the low SNR cases where the multipath interference is significantly weaker than background noise, the degree of correlation between adjacent correlation samples is determined mainly by the noise samples and is given approximately by $\gamma(\Delta T)$, where $\gamma(t)$ is expressed by (4).

2.2 Frequency-domain model

Taking the Fourier transform on (3) yields

$$Y(f) = Fd_m\sqrt{P}\sum_{l=1}^{L}\alpha_{l,m}\,\mathrm{e}^{\mathrm{j}(\varphi_{l,m}-2\pi f\tau_l)}\left|H(f)\right|^2 + N(f), \tag{9}$$

where $Y(f)$ and $N(f)$ are the Fourier transforms of $y(t)$ and $n(t)$, respectively. Therefore, when ΔT satisfies the Nyquist sampling criterion, the DFT bins of the selected correlation samples can be expressed as

$$\boldsymbol{x}_1(m) = \boldsymbol{A}\boldsymbol{s}(m) + \boldsymbol{n}_{f,1}(m), \quad m = 1, \ldots, M, \in \mathbb{C}^{(N\times 1)}, \tag{10}$$

where the lth column of $\boldsymbol{A}$ is given by

$$\boldsymbol{a}(\tau_l) = [\Gamma_1, \Gamma_2\,\mathrm{e}^{-\mathrm{j}2\pi\Delta f\tau_l}, \ldots, \Gamma_N\,\mathrm{e}^{-\mathrm{j}2\pi(N-1)\Delta f\tau_l}]^{\mathrm{T}} \tag{11}$$

with $\Gamma_n = \left|H((n-1)\Delta f)\right|^2$ and $\Delta f = 1/(N\Delta T)$. $\boldsymbol{n}_{f,1}(m)$ is a vector whose elements are the noise-plus-interference components in the frequency domain. The DFT bins expressed by (10) and (11) can be used to form snapshots in the frequency domain, which are called Type 1 in this paper. Unlike to the time-domain model, the adjacent elements of $\boldsymbol{n}_{f,1}(m)$ are rarely correlated with each other.

One of the useful features of frequency-domain processing is that covariance averaging can be employed, if needed, to recover the rank of the signal covariance matrix in coherent signal cases. Dividing each of the DFT bins with the signal spectrum Γ_n yields

$$\boldsymbol{x}_2(m) = \boldsymbol{A}\boldsymbol{s}(m) + \boldsymbol{n}_{f,2}(m), \quad m = 1, \ldots, M, \in \mathbb{C}^{(N\times 1)}, \tag{12}$$

where the lth column of $\boldsymbol{A} \in \mathbb{C}^{(N\times L)}$ is given by

$$\boldsymbol{a}(\tau_l) = [1, \mathrm{e}^{-\mathrm{j}2\pi\Delta f\tau_l}, \ldots, \mathrm{e}^{-\mathrm{j}2\pi(N-1)\Delta f\tau_l}]^{\mathrm{T}}. \tag{13}$$

The snapshots expressed by (12) and (13) are referred to as Type 2 in this paper. Since the signal spectrum is not flat, dividing the DFT bins with the signal spectrum increases the variances of the noise-plus-interference components around the spectrum boundary, especially when the SNR is very low. Therefore, the DFT bins around the boundary should be excluded from forming snapshots. Since $\boldsymbol{A}$ in (12) is a Vandermonde matrix, covariance averaging can be applied to recover the rank of the signal covariance matrix [29].

2.3 Sparse covariance model

Let $\{\tilde{\tau}_k\}_{k=1}^{K}$ denote a fine grid that covers the delays of interest. It is assumed that the signal delays lie on the grid (or at least very close to the grid). Then, we may express (6), (10), and (12) in an overcomplete form with $\boldsymbol{A} = [\boldsymbol{a}(\tilde{\tau}_1), \boldsymbol{a}(\tilde{\tau}_2), \ldots, \boldsymbol{a}(\tilde{\tau}_K)] \in \mathbb{C}^{(N\times K)}$ and $\boldsymbol{s}(m) = [s_1(m), s_2(m), \ldots, s_K(m)]^{\mathrm{T}} \in \mathbb{C}^{(K\times 1)}$. Since K is much greater than N, each equation is ill-posed and has infinitely many solutions. However, imposing the sparsity assumption on $\boldsymbol{s}$, the solution to each equation can be obtained uniquely and $\tilde{\tau}_k$ corresponding to the non-zero element s_k is accepted as one of the estimated delays of the signals.

In most of the hyperparameter-free sparse estimation algorithms, the covariance matrix and its estimate are involved in the cost function to be minimised. Assuming that the noise-plus-interference components are independent of each other, having equal variance σ^2, and that the signal components are uncorrelated with one another, the covariance matrix $\boldsymbol{R}$ is modelled as [19–23]

$$\boldsymbol{R} = \boldsymbol{A}\boldsymbol{P}\boldsymbol{A}^{\mathrm{H}} + \sigma^2\boldsymbol{I}_N, \tag{14}$$

where $\boldsymbol{R} \triangleq E[\boldsymbol{y}(m)\boldsymbol{y}^{\mathrm{H}}(m)]$ for time-domain methods and $\boldsymbol{R} \triangleq E[\boldsymbol{x}_i(m)\boldsymbol{x}_i^{\mathrm{H}}(m)]$, $i = 1, 2$, for frequency-domain methods, respectively, and $\boldsymbol{P} \triangleq E[\boldsymbol{s}(m)\boldsymbol{s}^{\mathrm{H}}(m)] = \mathrm{diag}(p_1, \ldots, p_K)$. In practice, however, the signals are highly correlated with one another or even coherent in multipath environments, so that the covariance matrix model expressed by (14) seems unreasonable for coherent signal cases. Nevertheless, most hyperparameter-free sparse algorithms employ this model since the power estimation based on (14) is not significantly influenced by the signal correlations [16, 19–22]. It should be also noted that the noise-plus-interference components at adjacent correlation samples are substantially correlated since the tap spacing ΔT is less than T_c. The tap spacing is normally set to $T_c/2$, considering both estimation performance and hardware complexity of a passive correlator. It was shown that the correlated noise-plus-interference components cause severe performance degradation in time-domain processing depending on the delays of the signals [26]. However, this undesired effect can be avoided in frequency-domain processing since the noise-plus-interference components at different DFT bins are rarely correlated with each other. Hence it can be said that the covariance matrix model expressed by (14) is better suited for frequency-domain processing.

3 Sparse parameter estimation-based TDE algorithms

3.1 SAMV

A series of iterative SAMV approaches that are based on the minimisation of the AMV criterion were originally proposed for DOA estimation. The AMV criterion to estimate the parameter $\boldsymbol{p}$ is given by [23, 30]

$$\hat{\boldsymbol{p}} = \arg\min_{\boldsymbol{p}}\,[\hat{\boldsymbol{r}} - \boldsymbol{r}(\boldsymbol{p})]^{\mathrm{H}}\boldsymbol{C}_r^{-1}[\hat{\boldsymbol{r}} - \boldsymbol{r}(\boldsymbol{p})] \tag{15}$$

with $\hat{\boldsymbol{r}} \triangleq \mathrm{vec}(\hat{\boldsymbol{R}})$, $\boldsymbol{r}(\boldsymbol{p}) \triangleq \mathrm{vec}(\boldsymbol{R})$, and $\boldsymbol{C}_r \triangleq E[\hat{\boldsymbol{r}}(\boldsymbol{p})\hat{\boldsymbol{r}}^{\mathrm{H}}(\boldsymbol{p})] = \boldsymbol{R}^* \otimes \boldsymbol{R}$. $\hat{\boldsymbol{R}}$ is the estimate of $\boldsymbol{R}$, which is given by $\hat{\boldsymbol{R}} = \boldsymbol{X}\boldsymbol{X}^{\mathrm{H}}/M$ with $\boldsymbol{X} = [\boldsymbol{y}(1), \boldsymbol{y}(2), \ldots, \boldsymbol{y}(M)]$ for time-domain processing and $\boldsymbol{X} = [\boldsymbol{x}_i(1), \boldsymbol{x}_i(2), \ldots, \boldsymbol{x}_i(M)]$, $i = 1, 2$, for frequency-domain processing, respectively. Also, $\boldsymbol{r}(\boldsymbol{p})$ is expressed as

$$\boldsymbol{r}(\boldsymbol{p}) = \bar{\boldsymbol{A}}\boldsymbol{p} \tag{16}$$

with $\bar{\boldsymbol{A}} \triangleq [\bar{\boldsymbol{a}}_1, \ldots, \bar{\boldsymbol{a}}_K, \bar{\boldsymbol{a}}_{K+1}]$, $\bar{\boldsymbol{a}}_k \triangleq \boldsymbol{a}_k \otimes \boldsymbol{a}_k$, $\bar{\boldsymbol{a}}_{K+1} \triangleq \mathrm{vec}(\boldsymbol{I}_{\tilde{N}})$, and $\boldsymbol{p} \triangleq [p_1, \ldots, p_K, \sigma^2]$. We use $\boldsymbol{a}_k$ instead of $\boldsymbol{a}(\tilde{\tau}_k)$ for notational simplicity. Performing vectorisation on the noise-plus-interference covariance matrix at $\tilde{\tau}_k$ yields [23]

$$\boldsymbol{r}'_k \triangleq \boldsymbol{r} - p_k\bar{\boldsymbol{a}}_k, \quad k = 1, 2, \ldots, K, \tag{17}$$

where $\boldsymbol{r} \triangleq \mathrm{vec}(\boldsymbol{R}(i))$. Inserting $\boldsymbol{r} = \boldsymbol{r}'_k + p_k\bar{\boldsymbol{a}}_k$ into (15), the following equivalent cost function is obtained as:

$$\begin{aligned} f(p_k) = {} & (\hat{\boldsymbol{r}} - p_k\bar{\boldsymbol{a}}_k)^{\mathrm{H}}\boldsymbol{C}_r^{-1}(i)(\hat{\boldsymbol{r}} - p_k\bar{\boldsymbol{a}}_k) - (\hat{\boldsymbol{r}} - p_k\bar{\boldsymbol{a}}_k)^{\mathrm{H}} \\ & \times \boldsymbol{C}_r^{-1}(i)\boldsymbol{r}'_k - \boldsymbol{r}'^{\mathrm{H}}_k\boldsymbol{C}_r^{-1}(i)(\hat{\boldsymbol{r}} - p_k\bar{\boldsymbol{a}}_k) + \boldsymbol{r}'^{\mathrm{H}}_k\boldsymbol{C}_r^{-1}(i)\boldsymbol{r}'_k \end{aligned} \tag{18}$$

where $\boldsymbol{C}_r(i) \triangleq \boldsymbol{R}^*(i) \otimes \boldsymbol{R}(i)$ and the solution of $\mathrm{d}f/\mathrm{d}p_k = 0$ is given by

$$\hat{p}_k = \frac{\bar{\boldsymbol{a}}_k^{\mathrm{H}}\boldsymbol{C}_r^{-1}(i)\hat{\boldsymbol{r}} + p_k\bar{\boldsymbol{a}}_k^{\mathrm{H}}\boldsymbol{C}_r^{-1}(i)\bar{\boldsymbol{a}}_k - \bar{\boldsymbol{a}}_k^{\mathrm{H}}\boldsymbol{C}_r^{-1}(i)\boldsymbol{r}}{\bar{\boldsymbol{a}}_k^{\mathrm{H}}\boldsymbol{C}_r^{-1}(i)\bar{\boldsymbol{a}}_k}. \tag{19}$$

Inserting $\bar{\boldsymbol{a}}_k \triangleq \boldsymbol{a}_k \otimes \boldsymbol{a}_k$, $\boldsymbol{r} \triangleq \mathrm{vec}(\boldsymbol{R}(i))$, $\hat{\boldsymbol{r}} \triangleq \mathrm{vec}(\hat{\boldsymbol{R}})$, and $p_k = \hat{p}_k(i)$ into the above equation and using the Kronecker matrix product operation, the power updating formulas based on the AMV criterion are obtained as follows [23]:

$$\begin{aligned} \hat{p}_k(i+1) = {} & \hat{p}_k(i) + \frac{\boldsymbol{a}_k^{\mathrm{H}}\boldsymbol{R}^{-1}(i)\hat{\boldsymbol{R}}\boldsymbol{R}^{-1}(i)\boldsymbol{a}_k}{\left[\boldsymbol{a}_k^{\mathrm{H}}\boldsymbol{R}^{-1}(i)\boldsymbol{a}_k\right]^2} \\ & - \frac{1}{\boldsymbol{a}_k^{\mathrm{H}}\boldsymbol{R}^{-1}(i)\boldsymbol{a}_k}, \quad k = 1, \ldots, K, \end{aligned} \tag{20}$$

$$\hat{\sigma}^2(i+1)=\frac{\mathrm{tr}[\boldsymbol{R}^{-2}(i)\hat{\boldsymbol{R}}]+\hat{\sigma}^2(i)\mathrm{tr}[\boldsymbol{R}^{-2}(i)]-\mathrm{tr}[\boldsymbol{R}^{-1}(i)]}{\mathrm{tr}[\boldsymbol{R}^{-2}(i)]}. \tag{21}$$

In the above equations, $\hat{p}_k(i)$ denotes the estimate of p_k at the ith iteration and $\boldsymbol{R}(i)$ is the matrix $\boldsymbol{R}$ made from $\hat{p}_k(i)$ and $\hat{\sigma}^2(i)$. It has been proved that the estimates obtained by (20) and (21) are identical to the ML estimate [23]. To avoid negative values, we can substitute $\hat{p}_k(i)=1/\boldsymbol{a}_k^{\mathrm{H}}\boldsymbol{R}^{-1}(i)\boldsymbol{a}_k$ and $\hat{\sigma}^2(i)=\mathrm{tr}[\boldsymbol{R}^{-1}(i)]/\mathrm{tr}[\boldsymbol{R}^{-2}(i)]$ into (20) and (21). Then, the updating formulas for SAMV to estimate the signal powers and noise variance are given as follows [23]:

$$\hat{p}_k(i+1)=\hat{p}_k(i)\frac{\boldsymbol{a}_k^{\mathrm{H}}\boldsymbol{R}^{-1}(i)\hat{\boldsymbol{R}}\boldsymbol{R}^{-1}(i)\boldsymbol{a}_k}{\boldsymbol{a}_k^{\mathrm{H}}\boldsymbol{R}^{-1}(i)\boldsymbol{a}_k},\quad k=1,\ldots,K, \tag{22}$$

$$\hat{\sigma}^2(i+1)=\frac{\mathrm{tr}[\boldsymbol{R}^{-2}(i)\hat{\boldsymbol{R}}]}{\mathrm{tr}[\boldsymbol{R}^{-2}(i)]}. \tag{23}$$

Initial estimates can be obtained by $\{\hat{p}_k(0)\}_{k=1}^K=\boldsymbol{a}_k^{\mathrm{H}}\hat{\boldsymbol{R}}\boldsymbol{a}_k/\parallel\boldsymbol{a}_k\parallel^4$ and $\hat{\sigma}^2(0)$ can be chosen arbitrarily small. The power update is terminated if the condition $\parallel\hat{\boldsymbol{p}}(i+1)-\hat{\boldsymbol{p}}(i)\parallel/\parallel\hat{\boldsymbol{p}}(i)\parallel<\eta_0$ is satisfied. The signal delays are then determined by searching the peaks of the power estimates $\hat{\boldsymbol{p}}$.

3.2 SPICE

The SPICE algorithm has two different covariance fitting criteria but in this paper we consider the following cost function [20]

$$g=\parallel\boldsymbol{R}^{-1/2}(\hat{\boldsymbol{R}}-\boldsymbol{R})\hat{\boldsymbol{R}}^{-1/2}\parallel^2, \tag{24}$$

which provides a statistically stronger motivation [20]. It was shown that the minimisation of g with respect to $\boldsymbol{p}$ is equivalent to the following constrained minimisation:

$$\min_{\{p_k\geq 0\}}\ \mathrm{tr}(\hat{\boldsymbol{R}}^{1/2}\boldsymbol{R}^{-1}\hat{\boldsymbol{R}}^{1/2})\quad \mathrm{s.t.}\quad \sum_{k=1}^{K+N}\omega_k p_k=1 \tag{25}$$

$$\omega_k=\boldsymbol{a}_k^{\mathrm{H}}\hat{\boldsymbol{R}}^{-1}\boldsymbol{a}_k/N. \tag{26}$$

The power updating formulas of SPICE are summarised as [20]:

$$\hat{p}_k(i+1)=\hat{p}_k(i)\frac{\parallel\boldsymbol{a}_k^{\mathrm{H}}\boldsymbol{R}^{-1}(i)\hat{\boldsymbol{R}}^{1/2}\parallel}{\omega_k^{1/2}\rho(i)},\quad k=1,\ldots,K, \tag{27}$$

$$\hat{\sigma}^2(i+1)=\hat{\sigma}^2(i)\frac{\parallel\boldsymbol{R}^{-1}(i)\hat{\boldsymbol{R}}^{1/2}\parallel}{\nu^{1/2}\rho(i)}, \tag{28}$$

$$\begin{aligned}\rho(i)=&\sum_{k=1}^{K}\omega_k^{1/2}\hat{p}_k(i)\parallel\boldsymbol{a}_k^{\mathrm{H}}\boldsymbol{R}^{-1}(i)\hat{\boldsymbol{R}}^{1/2}\parallel\\&+\nu^{1/2}\hat{\sigma}^2(i)\parallel\boldsymbol{R}^{-1}(i)\hat{\boldsymbol{R}}^{1/2}\parallel\end{aligned} \tag{29}$$

with $\nu=\sum_{k=1}^{K+N}\omega_k$. Initial estimates can be also obtained with the same methods as those for SAMV. Since SPICE with the cost function defined by (24) involves $\hat{\boldsymbol{R}}^{-1}$ in power estimation, it can be used only when the number of available snapshots is larger than or equal to the dimension of the snapshot vectors, i.e. $M\geq N$.

The frequency-domain SAMV and SPICE algorithms for TDE are summarised as follows:

(i) *Step 1*: Forming snapshots and initialisaion

- Select N correlation samples and perform N-point DFT.
- Select contiguous $\bar{N}$ DFT bins to form snapshots in (10) or (12) and apply covariance averaging, if needed.
- Obtain $\{\hat{p}_k(0)\}_{k=1}^K$ using $\boldsymbol{a}_k^{\mathrm{H}}\hat{\boldsymbol{R}}\boldsymbol{a}_k/\parallel\boldsymbol{a}_k\parallel^4$ and set an arbitrary small value for $\hat{\sigma}^2(0)$.

(ii) *Step 2*: Sparse estimation algorithms

- Update $\boldsymbol{R}(i)=\boldsymbol{A}\hat{\boldsymbol{P}}(i)\boldsymbol{A}^{\mathrm{H}}+\hat{\sigma}^2(i)\boldsymbol{I}_{\bar{N}}$.
- Update $\{\hat{p}_k(i+1)\}_{k=1}^K$ and $\hat{\sigma}^2(i+1)$ using (22) and (23) for SAMV or (27)–(29) for SPICE, respectively.
- Repeat the above process until convergence.

3.3 SAMV-WRELAX

The sparse parameter estimation methods require a sufficiently fine grid to attain high estimation accuracy, which causes large computational loads. If they employ a coarse grid simply to reduce computational loads, severe performance degradation may occur for off-grid signals. The computational loads of the sparse estimation methods can be reduced efficiently without any performance degradations if they are used in combination with the WRELAX algorithm [10]. WRELAX is a relaxation-based method that decouples a complicated multi-dimensional optimisation problem into a sequence of multiple one-dimensional optimisation problems [10, 11]. When the signals are not spaced very closely in arrival times, WRELAX usually converges in a few steps. However, when the signals are very closely spaced, it converges very slowly. The slow convergence of WRELAX can be avoided by using the time delay estimates obtained by the sparse estimation methods with a coarse grid as the initial values for the last step of WRELAX [10]. More accurate estimates are then obtained via WRELAX. We select the frequency-domain SAMV to provide the initial time delay estimates since it is superior to the time-domain SAMV and other sparse algorithms, which will be proved through the numerical examples in Section 4.

Once the estimates $\{\hat{\tau}_l\}_{l=1}^L$ are obtained, the signal amplitudes can be estimated by

$$\hat{\boldsymbol{S}}=(\hat{\boldsymbol{A}}^{\mathrm{H}}\hat{\boldsymbol{A}})^{-1}\hat{\boldsymbol{A}}^{\mathrm{H}}\boldsymbol{X}, \tag{30}$$

where $\hat{\boldsymbol{A}}=[\hat{\boldsymbol{a}}_1,\hat{\boldsymbol{a}}_2,\ldots,\hat{\boldsymbol{a}}_L]$ and $\hat{\boldsymbol{S}}=[\hat{\boldsymbol{s}}_1,\hat{\boldsymbol{s}}_2,\ldots,\hat{\boldsymbol{s}}_L]^{\mathrm{T}}$, and $\hat{\boldsymbol{s}}_l$ is the $M\times 1$ column vector denoting the amplitude estimates of the lth signal. The amplitude estimates given above can be poor when the delay estimates $\{\hat{\tau}_l\}_{l=1}^L$ are closely spaced since $\hat{\boldsymbol{A}}$ is seriously ill-conditioned. A simple spacing adjustment scheme was proposed to avoid this problem in [10]. If the spacing between any two estimates, say, $\hat{\tau}_1$ and $\hat{\tau}_2$ ($\hat{\tau}_1\leq\hat{\tau}_2$), is smaller than a pre-defined threshold $\Delta\tau$, we adjust the estimates by replacing $\hat{\tau}_1$ with $\hat{\tau}_1-0.5\Delta\tau$ and $\hat{\tau}_2$ with $\hat{\tau}_2+0.5\Delta\tau$. The signal amplitudes are then estimated by using the adjusted delay estimates.

Consider the following NLS criterion:

$$C_1(\{\boldsymbol{s}_l,\tau_l\}_{l=1}^L)=\parallel\boldsymbol{X}-\boldsymbol{A}\boldsymbol{S}\parallel^2. \tag{31}$$

Minimising (31) yields the ML estimator when the noise process is white Gaussian. However, minimising $C_1(\{\boldsymbol{s}_l,\tau_l\}_{l=1}^{l=L})$ with respect to the unknown parameters is a complicated multi-dimensional non-linear optimisation problem. Assuming that $\{\boldsymbol{s}_i,\tau_i\}_{i=1,i\neq l}$ are given, let

$$\boldsymbol{X}_l=\boldsymbol{X}-\tilde{\boldsymbol{A}}_l\boldsymbol{S} \tag{32}$$

where $\tilde{\boldsymbol{A}}_l$ denotes $\boldsymbol{A}$ with its lth column replaced with a zero vector. Then (31) equivalently becomes [10]

$$C_2(\{\boldsymbol{s}_l,\tau_l\})=\parallel\boldsymbol{X}_l-\tilde{\boldsymbol{A}}_l\boldsymbol{S}\parallel^2, \tag{33}$$

which is a one-dimensional optimisation problem with respect to $\boldsymbol{s}_l$ and τ_l. Minimising $C_2(\{\boldsymbol{s}_l,\tau_l\})$ yields [10]

$$\hat{\tau}_l = \arg\max_{\tau_l} \| \boldsymbol{a}_l^{\mathrm{H}} \boldsymbol{X}_l \|^2 \tag{34}$$

and

$$\hat{\boldsymbol{s}}_l = \left. \frac{\boldsymbol{a}_l^{\mathrm{H}} \boldsymbol{X}_l}{\| \boldsymbol{a}_l \|^2} \right|_{\tau_l = \hat{\tau}_l}. \tag{35}$$

Therefore, given $\{\hat{\boldsymbol{s}}_l, \hat{\tau}_l\}_{l=1}^{L}$, (34) and (35) can be regarded as the updates of $\hat{\boldsymbol{s}}_l$ and $\hat{\tau}_l$, and all the updates of $\{\hat{\boldsymbol{s}}_l, \hat{\tau}_l\}_{l=1}^{L}$ can be obtained by the same procedure. SAMV-WRELAX only requires a one-dimensional search with respective to the scalar τ_l, which can be efficiently implemented by the Nelder–Mead algorithm.

The SAMV-WRELAX algorithm is summarised as follows:

(i) *Step 1*: SAMV for initial estimates

- Apply SAMV to obtain $\{\hat{\tau}_l\}_{l=1}^{L}$.
- Adjust $\{\hat{\tau}_l\}_{l=1}^{L}$ so that the minimum spacing of $\{\hat{\tau}_l\}_{l=1}^{L}$ is at least a pre-defined $\Delta\tau$.
- Obtain $\{\hat{\boldsymbol{s}}_l\}_{l=1}^{L}$ using (30).

(ii) *Step 2*: Last step of WRELAX

- Compute $\boldsymbol{X}_1$ using $\{\hat{\tau}_l, \hat{\boldsymbol{s}}_l\}_{l=2}^{L}$ obtained in Step 1 and update $\{\hat{\tau}_1, \hat{\boldsymbol{s}}_1\}$ using (34) and (35).
- Compute $\boldsymbol{X}_2$ using $\{\hat{\tau}_l, \hat{\boldsymbol{s}}_l\}_{l=1, l\neq 2}^{L}$ and update $\{\hat{\tau}_2, \hat{\boldsymbol{s}}_2\}$ from $\boldsymbol{X}_2$.
- Continue this procedure until $\{\hat{\tau}_L, \hat{\boldsymbol{s}}_L\}$ are updated.
- Repeat the above process until convergence.

The convergence in the iterations of WRELAX may be determined by checking the relative changes of the cost function $C_1(\{\boldsymbol{s}_l, \tau_l\}_{l=1}^{L})$ in (31) between two consecutive iterations [10].

4 Numerical results and discussions

In order to evaluate the performances of the sparse parameter estimation methods discussed in Section 3, we apply them to the ISO/IEC 24730-2 RTLS (Part 21) that employs a differential BPSK data encoding and BPSK spreading scheme [1]. The period of the PN sequence is $511T_{\mathrm{c}}$, the chip rate is 30.521875 Mcps, and the data rate is 59.7 Kbps. The pulse-shaping filter and the corresponding matched filter are designed to have the same root-raised cosine filter with a roll-off factor of 0.98, which is selected to meet the requirement on the maximum occupied channel bandwidth of 60 MHz [1]. Baseband signal samples are generated with a period of $0.125T_{\mathrm{c}}$, which are fed into a passive correlator with a tap spacing of $0.5T_{\mathrm{c}}$ after matched filtering. Therefore, 1022 samples are obtained during each symbol period. The sampling rate and the tap spacing were selected by considering both the demodulator performance and the H/W complexity. It is assumed that there are three signals with equal strength and that the strength of each signal is constant for all numerical examples. For coherent signal cases, the phase differences of the three signals are kept constant with initial phases 0°, 90°, 270°, respectively, while for uncorrelated signal cases, the phase of each signal is randomly changed over $(0°, 360°)$ every symbol. The first 16 correlation samples are selected to cover up to the delay of $8T_{\mathrm{c}}$, which corresponds to the maximum distance of 80 m between tags and readers. The number of snapshots is set to 50 by considering the minimum packet length of the RTLS. The grid is also set to cover the delays of interest with a grid size of $0.01T_{\mathrm{c}}$. Unless otherwise specified, 13 contiguous DFT bins from the 3rd to 15th bin of the double-sided spectrum are selected for all the frequency-domain approaches. Type 1 snapshots are employed for the frequency-domain SAMV since SAMV is robust to the signal correlation, thereby not requiring covariance averaging. On the other hand, SPICE is highly sensitive to the signal correlation, so Type 2 snapshots are used for the frequency-domain SPICE to employ covariance averaging. The number of sub-groups is set to three for covariance averaging. The power update is set to terminate if the condition $\| \hat{\boldsymbol{p}}(i+1) - \hat{\boldsymbol{p}}(i) \| / \| \hat{\boldsymbol{p}}(i) \| < 10^{-3}$ is satisfied.

Fig. 2 shows the TDE results of the sparse parameter estimation methods in the case where there are three coherent signals. Each signal has a delay $\tau_1 = 1.75T_{\mathrm{c}}$, $\tau_2 = 2.25T_{\mathrm{c}}$, and $\tau_3 = 3.875T_{\mathrm{c}}$, respectively. The input SNR of each signal is −10 dB, which is defined by $PT_{\mathrm{c}}E[\alpha_l^2(t)]/N_{\mathrm{o}}$. Each figure is the superposition of 20 Monte Carlo runs. The dashed lines denote the true delays of the signals. In the figures, the prefixes TD and FD were used to represent the time- and frequency-domain approaches, respectively. It is observed that the frequency-domain SAMV employing Type 1 snapshots provides better resolution than the time-domain SAMV, whereas the frequency-domain SPICE employing Type 2 snapshots performs significantly better than the time-domain SPICE. It has been demonstrated that SAMV is robust to the signal correlation [26], so that the rank recovery of the signal covariance contributes hardly to performance improvement. Moreover, dividing the selected DFT bins with the signal spectrum may cause performance degradation by deemphasising the high SNR DFT bins. Contrary to the SAMV approaches, however, the performances of the SPICE approaches depend largely on the signal correlation, so that the performance of the frequency-domain SPICE is significantly improved by covariance averaging in coherent signal cases. It should be also noted that the time-domain approaches exhibit significant spurious peaks, which are due mainly to the correlated noise-plus-interference components, which may cause serious estimation errors depending on the delays of the signals. Moreover, the time-domain SPICE suffers from a serious decrease of spectral peaks for the coherent signal cases, thereby its performance is more severely affected by the spurious peaks.

Fig. 3 shows the root mean square (RMS) errors of the delay estimates versus input SNR for various delays of Signals 1 and 2 in the case where there are three coherent signals, with Fig. 3*a* for the SAMV approaches and Fig. 3*b* for the SPICE approaches, respectively. The signal delays were changed from $\tau_1 = 1.375T_{\mathrm{c}}$, $\tau_2 = 1.875T_{\mathrm{c}}$ to $\tau_1 = 2.0T_{\mathrm{c}}$, $\tau_2 = 2.5T_{\mathrm{c}}$ with an increment of $0.125T_{\mathrm{c}}$, while the delay difference between Signals 1 and 2 was maintained to be $0.5T_{\mathrm{c}}$. The delay of Signal 3 was fixed at $3.875T_{\mathrm{c}}$. $\bar{K} = 200$ Monte Carlo runs were performed to obtain the RMS errors at each SNR. The RMS errors were calculated by $\sqrt{(1/\bar{K})\sum_{i=1}^{2}\sum_{k=1}^{\bar{K}}(\hat{\tau}_{i,k} - \tau_i)^2}$, where τ_i, $i = 1, 2$ are the true delays of the ith signal, and $\hat{\tau}_{i,k}$, $i = 1, 2, k = 1, \ldots, \bar{K}$ are the kth estimate of the ith signal, respectively. In the figures, the solid lines represent the mean values of the RMS errors obtained with different delay sets, while the symbols at upper and lower sides denote the maximum and minimum RMS errors, respectively, for a given SNR. It is observed that the frequency-domain SPICE performs significantly better than the time-domain SPICE, whereas the performance of the frequency-domain SAMV is slightly improved compared to the time-domain SAMV in terms of the mean value. It should be noted that the performances of the time-domain approaches depend largely on the signal delays, which is due mainly to the spurious peaks as shown in Fig. 2. In the time-domain approaches, as discussed earlier, the noise-plus-interference components in adjacent correlation samples are substantially correlated with each other, which causes more severe and densely clustered spurious peaks. In this example, the degree of correlation between adjacent noise-plus-interference components is approximately given by $\gamma(0.5T_{\mathrm{c}}) = 0.67$ when the input SNR is very low. On the contrary, the performances of the frequency-domain approaches depend little on the signal delays at low SNR cases since the noise-plus-interference components at different DFT bins are hardly correlated. The large deviation of the RMS errors at high SNR situations is due mainly to the grid size limitation.

Fig. 4 shows the RMS errors versus input SNR in uncorrelated signal cases. All simulation conditions other than the signal correlation are the same as those for Fig. 3. Comparing Figs. 3*a* and 4*a*, we can observe that the SAMV approaches are very robust to the signal correlation in both the time and frequency domains. As for the SPICE approaches, however, time-domain processing

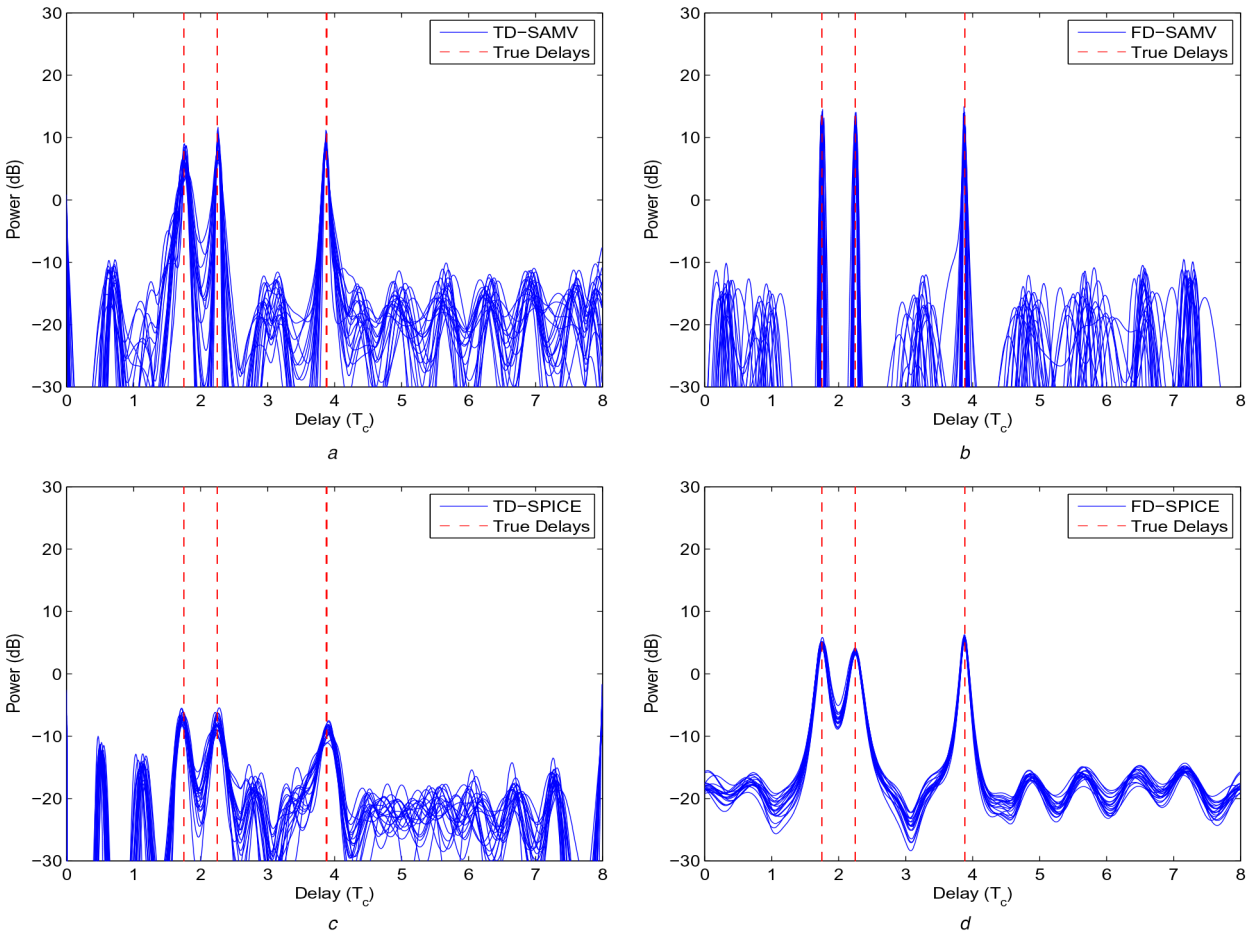

Fig. 2 *TDE results in coherent signal cases (SNR = −10 dB, $\Delta_{1,2} = 0.5T_c$)*

(a) Time-domain SAMV, ***(b)*** Frequency-domain SAMV employing Type 1 snapshots, ***(c)*** Time-domain SPICE, ***(d)*** Frequency-domain SPICE employing Type 2 snapshots

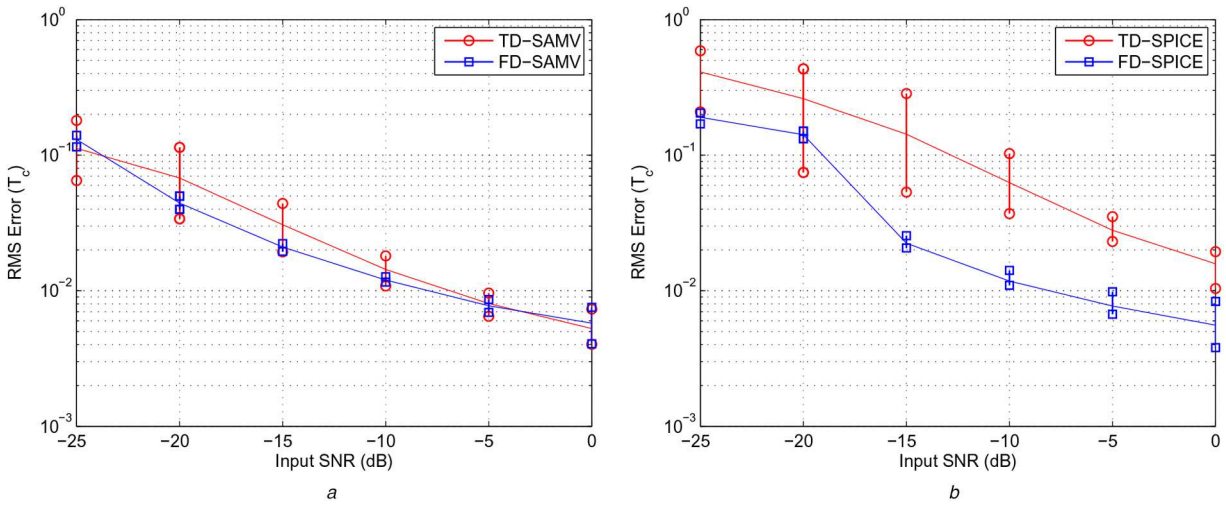

Fig. 3 *RMS errors versus input SNR for various delays of Signals 1 and 2 in coherent signal cases ($\Delta_{1,2} = 0.5T_c$)*

(a) SAMV approaches, ***(b)*** SPICE approaches

performs significantly better in uncorrelated signal cases, whereas frequency-domain processing provides similar performances regardless of the signal correlation. Fig. 4 also illustrates that each of the frequency-domain approaches performs better than the corresponding time-domain approach, which is due to the fact that the noise-plus-interference components at different DFT bins are independent. In the low SNR situations of below −15 dB, the frequency-domain SAMV provides better performance than the frequency-domain SPICE regardless of the signal correlation, while at the SNRs higher than −15 dB, they perform very similarly.

Fig. 5 shows the RMS errors versus input SNR in coherent signal cases where the time of arrival difference between Signals 1 and 2 is closely spaced by $0.25T_c$. The delays of Signals 1 and 2 were changed from $\tau_1 = 1.375T_c$, $\tau_2 = 1.625T_c$ to $\tau_1 = 2.0T_c$, $\tau_2 = 2.25T_c$ with an increment of $0.125T_c$. The delay of Signal 3 was fixed at $3.875T_c$. All other conditions are the same as those for Fig. 3. It is observed that the frequency-domain approaches again outperform the corresponding time-domain approaches. The performance of the time-domain SPICE improves very gradually in closely spaced signal cases as the SNR increases, which is because the resolution of the time-domain SPICE is poor for coherent signals. The SNR lower bound to resolve Signals 1 and 2 is close to −15 dB for the frequency-domain SAMV, but approximately −8 dB for the frequency-domain SPICE. The frequency-domain

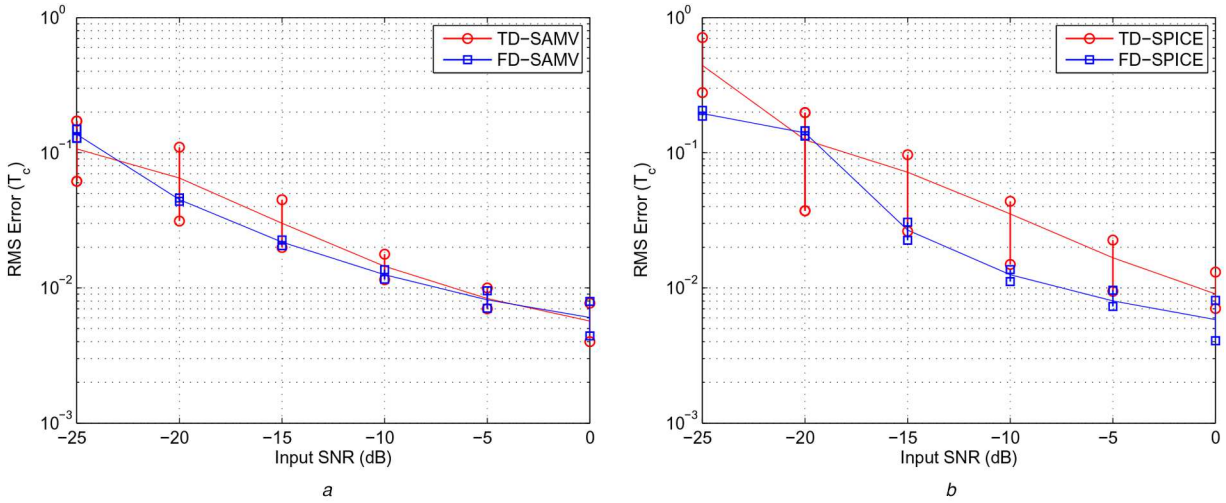

Fig. 4 *RMS errors versus input SNR for various delays of Signals 1 and 2 in uncorrelated signal cases ($\Delta_{1,2} = 0.5T_c$)*
(a) SAMV approaches, ***(b)*** SPICE approaches

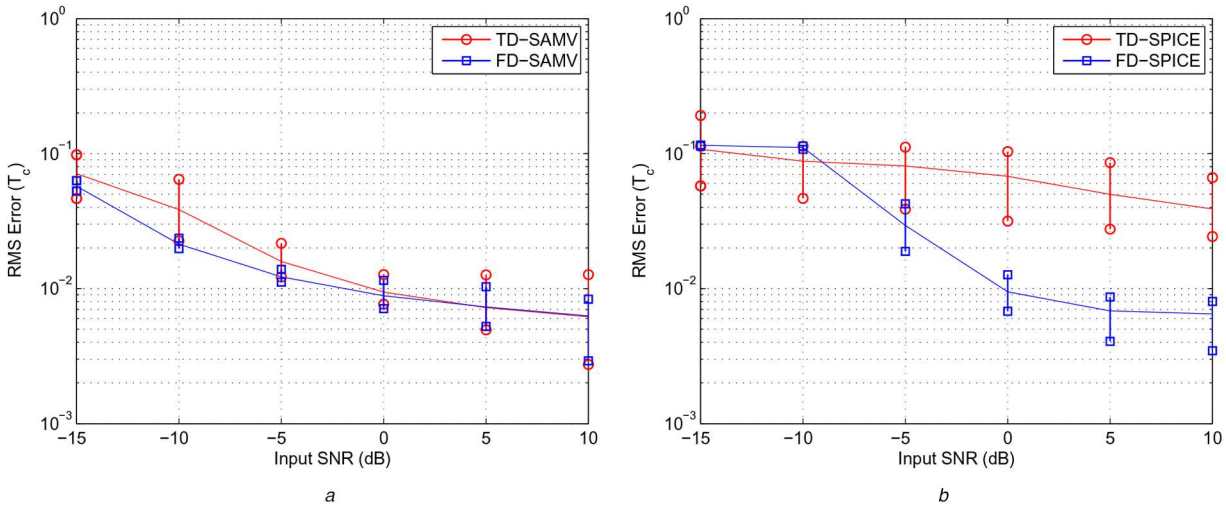

Fig. 5 *RMS errors versus input SNR for various delays of Signals 1 and 2 in coherent signal cases ($\Delta_{1,2} = 0.25T_c$)*
(a) SAMV approaches, ***(b)*** SPICE approaches

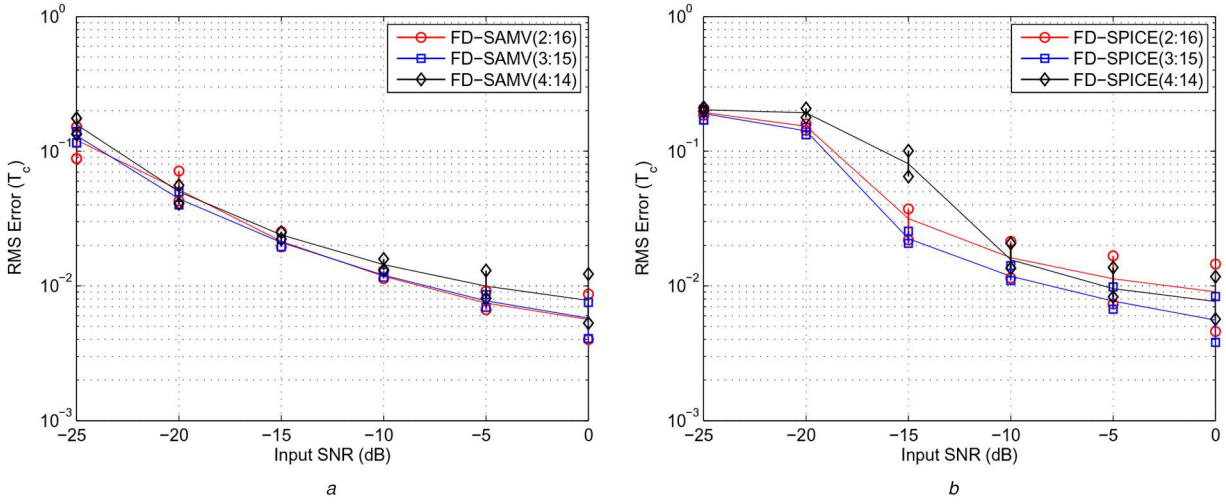

Fig. 6 *RMS errors versus input SNR for various selections of the DFT bins in coherent signal cases ($\Delta_{1,2} = 0.5T_c$)*
(a) Frequency-domain SAMV, ***(b)*** Frequency-domain SPICE

SAMV performs significantly better than the frequency-domain SPICE at the SNRs below 0 dB, while they perform similarly at the SNRs higher than 0 dB.

Fig. 6 illustrates the performances of the frequency-domain approaches for various selections of the DFT bins to form snapshots, with Fig. 6*a* for SAMV and Fig. 6*b* for SPICE, respectively. Three sets of contiguous DFT bins were used to form snapshots; the 2nd to 16th, 3rd to 15th, and 4th to 14th DFT bins. All other conditions are the same as those used for Fig. 3. It is observed that SPICE is more sensitive to the selection of the DFT bins than SAMV, which is because the noise variance increases severely around the boundary of the signal spectrum in Type 2

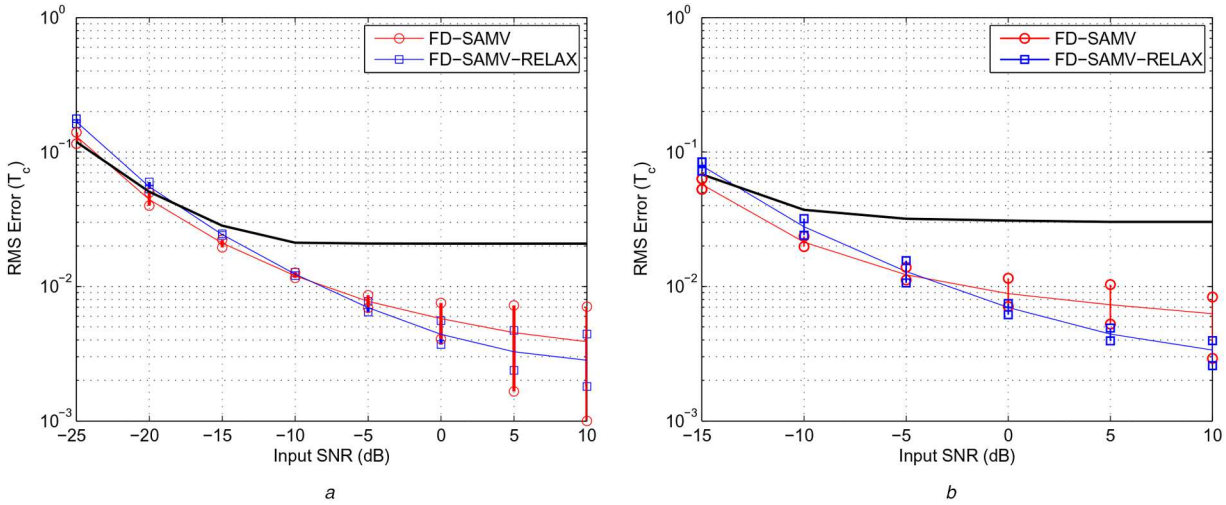

Fig. 7 *Comparison of RMS errors between SAMV and SAMV-RELAX*
(a) $\Delta_{1,2} = 0.5T_c$, ***(b)*** $\Delta_{1,2} = 0.25T_c$

snapshot cases. To avoid a severe increase of the noise variance, the DFT bins around the boundary should be excluded from forming snapshots, which, however, may reduce the resolution capability of SPICE. Moreover, covariance averaging for rank recovery further decreases the resolution of SPICE. On the contrary, in Type 1 snapshots, neither the noise variance increase nor the reduction in resolution due to covariance averaging arises. In addition, the DFT bins around the boundary contribute rarely to performance improvement since their SNRs are much lower than those around the centre. Therefore, the performance of SAMV is little influenced by the selection of the DFT bins unless the number of selected DFT bins is unreasonably small. It is shown that the selection of the 3rd to 15th DFT bins provides the best performance for both SAMV and SPICE.

So far, the grid size was set to $0.01T_c$ solely to compare the performances of the sparse parameter estimation methods. With this fine grid, the sparse estimation methods become computationally very intensive. Moreover, the grid size limitation also causes a performance degradation at high SNR scenarios due to the off-grid effect. Fig. 7 shows the time delay estimates of the frequency-domain SAMV and SAMV-WRELAX with Fig. 7*a* for $\Delta_{1,2} = 0.5T_c$ and Fig. 7*b* for $\Delta_{1,2} = 0.25T_c$, respectively. The grid size was set to $0.01T_c$ for SAMV and $0.1T_c$ for SAMV-WRELAX, respectively. The time spacing and update thresholds for WRELAX were set to $0.2T_c$ and 10^{-3}, respectively. In the figures, the black solid lines represent the means of the RMS values when SAMV employs the grid size of $0.1T_c$. It is observed that SAMV-WRELAX performs better than SAMV with a fine grid at high SNR scenarios, while performing slightly worse at low SNR cases. However, the computational load of SAMV-WRELAX decreases up to a few tenths of that of SAMV with a fine grid. It is also observed that SAMV suffers from the plateau effect, which is more serious for a coarse grid case. The time-domain SAMV or other sparse estimation methods such as SPICE and IAA can be also considered for use in combination with WRELAX. However, since they are inferior to the frequency-domain SAMV especially at low SNR scenarios, their combinations with WRELAX also perform worse than SAMV-WRELAX.

5 Conclusion

In this paper, two representative sparse parameter estimation methods, SAMV and SPICE have been extended to achieve the high-resolution TDE in both the time and frequency domains and their performances have been evaluated in various multipath environments. A combined approach of the frequency-domain SAMV and WRELAX has been also proposed to reduce the computational load. Numerical examples have demonstrated that the frequency-domain approaches with a proper type of snapshots outperform the corresponding time-domain approaches and mitigate the noise correlation problem encountered in time-domain processing. The computational load of SAMV-WRELAX with a grid size of $0.1T_c$ decreases up to a few tenths of that of SAMV with a grid size of $0.01T_c$ without any performance degradations.

6 References

[1] ISO/IEC 24730-2: 'Information technology – real time locating systems (RTLS) – part 2: direct sequence spread spectrum (DSSS) 2.4 GHz air interface protocol', 2012

[2] Ge, F.X., Shen, D., Peng, Y., *et al.*: 'Super-resolution time delay estimation in multipath environments', *IEEE Trans. Circuits Syst.*, 2007, **54**, (9), pp. 1977–1986

[3] Bouchereau, F., Brady, D., Lanzl, C.: 'Multipath delay estimation using a superresolution PN-correlation method', *IEEE Trans. Signal Process.*, 2001, **49**, (5), pp. 1194–1208

[4] Pallas, M.A., Jourdain, G.: 'Active high resolution time delay estimation for large BT signals', *IEEE Trans. Signal Process.*, 1991, **39**, (4), pp. 781–788

[5] Gedalyahu, K., Eldar, Y.C.: 'Time-delay estimation from low-rate samples: a union of subspaces approach', *IEEE Trans. Signal Process.*, 2010, **58**, (6), pp. 3017–3031

[6] Qu, L., Sun, Q., Yang, T., *et al.*: 'Time-delay estimation for ground penetrating radar using ESPRIT with improved spatial smoothing technique', *IEEE Geosci. Remote Sens. Lett.*, 2014, **11**, (8), pp. 1315–1319

[7] Falsi, C., Dardari, D., Mucchi, L., *et al.*: 'Time of arrival estimation for UWB localizers in realistic environments', *EURASIP J. Adv. Signal Process.*, 2006, **2006**, p. 1664. Available at https://doi.org/10.1155/ASP/2006/32082

[8] Seco-Granados, G., Fernandez-Rubio, J.A., Fernandez-Prades, C.: 'ML estimator and hybrid beamformer for multipath and interference mitigation in GNSS receivers', *IEEE Trans. Signal Process.*, 2005, **53**, (3), pp. 1194–1208

[9] Benesty, J., Huang, Y., Chen, J.: 'Time delay estimation via minimum entropy', *IEEE Signal Process. Lett.*, 2007, **14**, (3), pp. 157–160

[10] Wu, R., Li, J., Liu, Z.S.: 'Super resolution time delay estimation via MODE-WRELAX', *IEEE Aerosp. Electron. Syst.*, 1999, **35**, (1), pp. 294–307

[11] Li, J., Wu, R.: 'An efficient algorithm for time delay estimation', *IEEE Trans. Signal Process.*, 1998, **46**, (8), pp. 2231–2235

[12] Wax, M., Kailath, T.: 'Detection of signals by information theoretic criterion', *IEEE Trans. Acoust. Speech Signal Process.*, 1985, **33**, (2), pp. 387–392

[13] Tibshirani, R.: 'Regression shrinkage and selection via the LASSO', *J. R. Statist. Soc.*, 1996, **58**, (1), pp. 267–288

[14] Wang, L.: 'The L1 penalized LAD estimator for high dimensional linear regression', *J. Multivar. Anal.*, 2013, **120**, pp. 135–151

[15] Tan, X., Roberts, W., Li, J., *et al.*: 'Sparse learning via iterative minimization with application to MIMO radar imaging', *IEEE Trans. Signal Process.*, 2011, **59**, (3), pp. 1088–1101

[16] Roberts, W., Stoica, P., Li, J., *et al.*: 'Iterative adaptive approaches to MIMO radar imaging', *IEEE J. Sel. Top. Signal Process.*, 2010, **4**, (1), pp. 5–20

[17] Gorodnitsky, I.F., Rao, B.D.: 'Sparse signal reconstruction from limited data using FOCUSS: a re-weighted minimum norm algorithm', *IEEE Trans. Signal Process.*, 1997, **45**, (3), pp. 600–616

[18] He, Z.Q., Shi, Z.P., Huang, L., *et al.*: 'Underdetermined DOA estimation for wideband signals using robust sparse covariance fitting', *IEEE Signal Process. Lett.*, 2015, **22**, (4), pp. 435–438

[19] Yardibi, T., Li, J., Stoica, P., *et al.*: 'Source localization and sensing: a nonparametric iterative adaptive approach based on weighted least squares', *IEEE Trans. Aerosp. Electron. Syst.*, 2010, **46**, (1), pp. 425–443

[20] Stoica, P., Prabhu, B., Li, J.: 'SPICE: a sparse covariance-based estimation method for array processing', *IEEE Trans. Signal Process.*, 2011, **59**, (2), pp. 629–638

[21] Stoica, P., Prabhu, B., Li, J.: 'New method of sparse parameter estimation in separable models and its use for spectral analysis of irregularly sampled data', *IEEE Trans. Signal Process.*, 2011, **59**, (1), pp. 35–47

[22] Stoica, P., Zachariah, D., Li, J.: 'Weighted SPICE: a unifying approach for hyperparameter-free sparse estimation', *Digit. Signal Process.*, 2014, **33**, (6), pp. 1–12
[23] Abeida, H., Zhang, Q., Li, J.*, et al.*: 'Iterative sparse asymptotic minimum variance based approaches for array processing', *IEEE Trans. Signal Process.*, 2013, **61**, (4), pp. 933–944
[24] Sturm, J.: 'Using SeDuMi 1.02, a MATLAB toolbox for optimization over symmetric cones', *Optim. Methods Softw.*, 1999, **11**, (1), pp. 625–653
[25] Park, H.R., Li, J.: 'Sparse covariance-based high resolution time delay estimation for spread spectrum signals', *Electron. Lett.*, 2015, **51**, (2), pp. 155–157
[26] Park, H.R., Li, J.: 'Hyperparameter-free sparse signal reconstruction approaches to high resolution time delay estimation', *IEICE Trans. Commun.*, 2018, **E101-B**, (8), pp. 1809–1819
[27] Park, H.R., Li, J.: 'A frequency-domain SPICE approach to high-resolution time delay estimation', *IEEE Wirel. Commun. Lett.*, 2018, **7**, (3), pp. 360–363
[28] Viterbi, A.J.: '*CDMA: principles of spread spectrum communication*' (Addison-Wesley, USA, 1995)
[29] Williams, R.T., Prasad, S., Mahalanabis, A.K.*, et al.*: 'An improved spatial smoothing technique for bearing estimation in a multipath environment', *IEEE Trans. Acoust. Speech Signal Process.*, 1988, **36**, (4), pp. 425–432
[30] Abeida, H., Delma, J.P.: 'Efficiency of subspace-based DOA estimators', *Signal Process.*, 2007, **87**, (9), pp. 2075–2084